

Avalanches injecting flux into the central hole of a superconducting MgB₂ ring

Åge Andreas Falnes Olsen,* Tom Henning Johansen,† and Daniel Shantsev

Department of Physics and Center for Advanced Materials and Nanotechnology, University of Oslo, P.O. Box 1048 Blindern, 0316 Oslo, Norway

Eun-Mi Choi, Hyun-Sook Lee, Hyun Jung Kim, and Sung-Ik Lee

National Creative Research Initiative Center for Superconductivity, Department of Physics, Pohang University of Science and Technology, Pohang 790-784, Republic of Korea

(Received 31 March 2007; published 17 July 2007)

Magneto-optical imaging was used to observe dendritic flux avalanches connecting the outer and inner edges of a ring-shaped superconducting MgB₂ film. Such avalanches create heated channels across the entire width of the ring, and inject large amounts of flux into the central hole. By measuring the injected flux and the corresponding reduction of current, which is typically 15%, we estimate the maximum temperature in the channel to be 100 K, and the duration of the process to be on the order of a microsecond. Flux creep simulations reproduce all the observed features in the current density before and after injection events.

DOI: 10.1103/PhysRevB.76.024510

PACS number(s): 74.70.Ad, 74.25.Qt, 74.25.Ha, 74.78.Db

I. INTRODUCTION

In recent years it has become clear that instabilities are commonplace when magnetic flux penetrates superconductors. In particular, magnetic flux avalanches can abruptly penetrate thin superconducting samples in the form of tree or fingerlike patterns known as dendrites. Such avalanches were reported almost 15 years ago in YBa₂Cu₃O_x, where they must be triggered by a sudden pointlike heat pulse.^{1,2} Since then spontaneous dendritic avalanches have been observed³⁻⁷ in Nb, Nb₃Sn, YNi₂B₂C, and NbN, as well as in patterned Pb thin films.⁸ The recent interest in the phenomenon was largely triggered by the discovery⁹ that in MgB₂ films the avalanches are ubiquitous below a threshold temperature $T_{th} \sim 10$ K. The dendrites disrupt electrical current flow and limit the overall current capacity of superconductors,¹⁰ and are thus harmful for prospective applications. On the other hand, they also represent fertile ground for fundamental research as there exist many interesting challenges in understanding their nucleation and growth.

The dendritic instability is now believed to be of thermomagnetic origin. Motion of flux in superconductors releases heat and increases the temperature. Flux motion is facilitated by the increase in temperature, so more flux moves which then leads to even more heating. If the released heat is not transported away fast enough, an instability develops whereby large amount of magnetic flux rushes into the sample. This mechanism was originally invoked to explain global flux jumps where the entire sample is filled with a sudden burst of magnetic flux and all magnetization is lost.¹¹⁻¹³ However, the mechanism has recently also been shown to give localized, fingering instabilities.^{14,15} Indeed, the instability threshold field predicted from this model was recently¹⁶ shown to agree quantitatively with measurements in both Nb and MgB₂ films.

The dynamics of dendritic avalanches is extremely challenging to probe experimentally because of the short times involved. Typically the entire process of nucleation and growth of a single flux dendrite lasts a few hundred nanoseconds as measured using a sophisticated magneto-optical

(MO) setup.^{1,2} It is particularly difficult to measure the expected increase in temperature associated with the avalanches. On the other hand, it is possible to estimate the temperature in the dendrite indirectly by designing a suitable geometry where dendritic avalanches can leave a long-lasting, temperature dependent imprint. In particular, in superconducting rings dendrites may span the entire ring width and thus create a heated channel that connects the inner and outer edges. During the brief time that this channel is open it injects flux into the otherwise screened central hole in a process which may be described as magnetic perforation. This process depends on the temperature in the channel, which may then be inferred from measurements of the flux contained in the hole.

In this paper we report a detailed study on the perforation process in a superconducting MgB₂ ring using MO imaging. The technique, described in Sec. II, provides us with a detailed map of the flux distribution over a sample-wide area. In Sec. III we present our experimental results, showing the evolution of the flux $\Phi_{r < r_p}$ contained within the screened region $r < r_p$ during field ramps at different temperatures. The radius r_p is where the flux fronts from the inner and outer edges meet at full penetration. $\Phi_{r < r_p}$ displays abrupt jumps when dendrites cross the ring. We also calculate the current distribution based on the obtained field maps. From a simple model presented in Sec. IV which connects the temperature evolution in the heated channel with the evolution of the current during perforations we estimate the peak temperature during flux injection. We find that this temperature is $2.5T_c$, and that the duration of the flux injection process is on the order of one μ s. Finally, in Sec. V we propose a numerical model to describe how the perforation affects the current distribution in the ring.

II. EXPERIMENTAL SETUP

A MgB₂ film was prepared by pulsed laser deposition on a sapphire substrate. Details of the manufacturing process and typical properties of the superconductor can be found

elsewhere.^{17,18} Using photolithography the superconducting film of thickness $d=0.5\ \mu\text{m}$ was patterned into a ring with inner radius $r_0=1.10\ \text{mm}$ and outer radius $r_1=2\ \text{mm}$.

The magneto-optical indicator was a ferrite garnet film of thickness $5\ \mu\text{m}$ grown on a gadolinium gallium garnet substrate and covered with an Al mirror. Monodisperse beads (diameter $3.5\ \mu\text{m}$) were sprinkled on the sample to ensure a small and uniform distance between the superconductor and the Al mirror prior to positioning of the indicator. This precaution is necessary since metallic layers are known to suppress dendritic avalanches^{19,18} in MgB_2 . The entire stack was mounted in an optical cryostat (a liquid helium flow cryostat from Oxford Instruments) and cooled to low temperature for observation in a polarization microscope. We ensured sensitivity to field direction by setting the polarizer-analyzer angle α a few degrees away from full extinction. Images were captured with a QImaging Retiga Exi CCD camera with 12-bit pixel depth, controlled from a computer. The coil current was controlled from the same computer by means of a DAC card used to generate a control voltage to the current source. The computer also communicated with an external voltmeter (Hewlett Packard 34401A), which was used to monitor the coil current. The experiments were then conducted by slowly ramping the applied field from 0 to 25 mT while recording 50–200 images at regular intervals. Each time an image was recorded, the coil current was read and written to a log file before proceeding with the field ramp.

We calibrated image brightness to field by capturing 20–30 images at low temperature of an area away from the sample, while ramping the applied field from 0 to 40 mT. The recorded applied field and the image brightness were used to fit a second-degree polynomial $I(B)=a_2B^2+a_1B+a_0$ relating magnetic field to the image intensity. This polynomial form follows from Malus law for light intensity in a polarization microscope

$$I = I_0 \sin^2(\theta + \alpha) + I_b \quad (1)$$

along with the phenomenological linear relation $\theta \propto B$ for the Faraday rotation at small angles.

The calibration was performed pixel-by-pixel, which is necessary to account for uneven illumination in the field of view. The raw images were then processed in two stages: first, each image was converted to a field map using the obtained values of the fitting coefficients $\{a_i\}$ and secondly the flux $\Phi_{r < r_p}$ was computed by summing the field at each pixel contained within the relevant region.

Sensor noise leads to observable noise in the field values computed for each pixel, but summing over many thousand pixels to obtain the flux in a region effectively reduces random noise to insignificant levels. A more serious concern in quantitative magneto-optical measurements is systematic errors (see Ref. 20), particularly the existence of in-plane domains in indicator films which show up as triangular features of brighter and darker areas. The domain boundaries move easily in response to changes in temperature and applied field, and therefore result in a changing background. We minimized their influence by mounting the indicator very carefully on the sample to avoid mechanical stresses, and by applying a weak in-plane field. Despite these precautions do-

main splitting did occur in the experiments presented here. This was observed as dark regions slowly moving into the field of view during the field ramps, thus leading us to calculate a too low field value in the affected pixels. Fortunately, visual inspection of the images reveals that only a small part of the interesting region is affected, never more than $\approx 10\%$ of the total area.

III. EXPERIMENTAL RESULTS

Figure 1(a) shows an example field map recorded at $T=6.2\ \text{K}$ after applying a perpendicular field to the zero-field-cooled sample. Notice the negative field at the inner ring edge which is the accumulated stray field from the supercurrents. In the lower left quadrant of the ring we observe one of the relatively few, but also relatively large, dendrites formed at this temperature. In fact, the image shown here was the last taken prior to the nucleation and growth of a second dendrite which spanned the entire ring width and injected large amounts of flux into the central hole. This perforation event is illustrated in Fig. 1(b) showing the difference between the frame in (a) and the subsequent frame taken at a slightly larger field. The increase in flux inside the central hole, and the accompanying reduction near the outer edge, are evident: the dendrite brings large amounts of flux from outside the sample into the central hole. Remarkably, as dramatic as the perforation event is, the flux distribution inside the superconducting material is left largely unchanged in the process.

Well below the threshold temperature T_{th} we observe more frequent dendritic avalanches. At $T=3.8\ \text{K}$ the first dendrite appears at roughly $B_a=5\ \text{mT}$. As reported previously²¹ the size of individual dendrites increases with the applied field, until they span the entire ring and cause perforations.

For low applied fields, before the first perforation event occurs, the superconductor screens the area contained within r_p , a characteristic radius where the flux fronts from the outer and inner edges meet in a critical state superconducting ring. The flux inside this region, $\Phi_{r < r_p}$, is the sum of the contributions from the supercurrents Φ_{self} and the applied field $\Phi_{B_a} = B_a A_{r < r_p}$:

$$\Phi_{r < r_p} = B_a A_{r < r_p} + \Phi_{\text{self}}. \quad (2)$$

Provided no perforations have occurred and the applied field is below the field of full penetration B_p , this sum is exactly zero. Figure 2 shows the evolution of $\Phi_{r < r_p}$ during ramps of the applied field at four different temperatures. For the highest temperature $T=7\ \text{K}$ (above the threshold T_{th} for the onset of dendritic avalanches in the present experiment) the flux remains zero until the applied field reaches B_p , after which it increases linearly with the applied field. The crossover results from the fact that the current in the superconductor has saturated and hence the term Φ_{self} remains essentially constant when the applied field is increased further. The light gray oblique lines in Fig. 2 show slopes expected from the $B_a A_{r < r_p}$ term. Guided by these lines one can see that the slope of the measured curve is slightly larger than

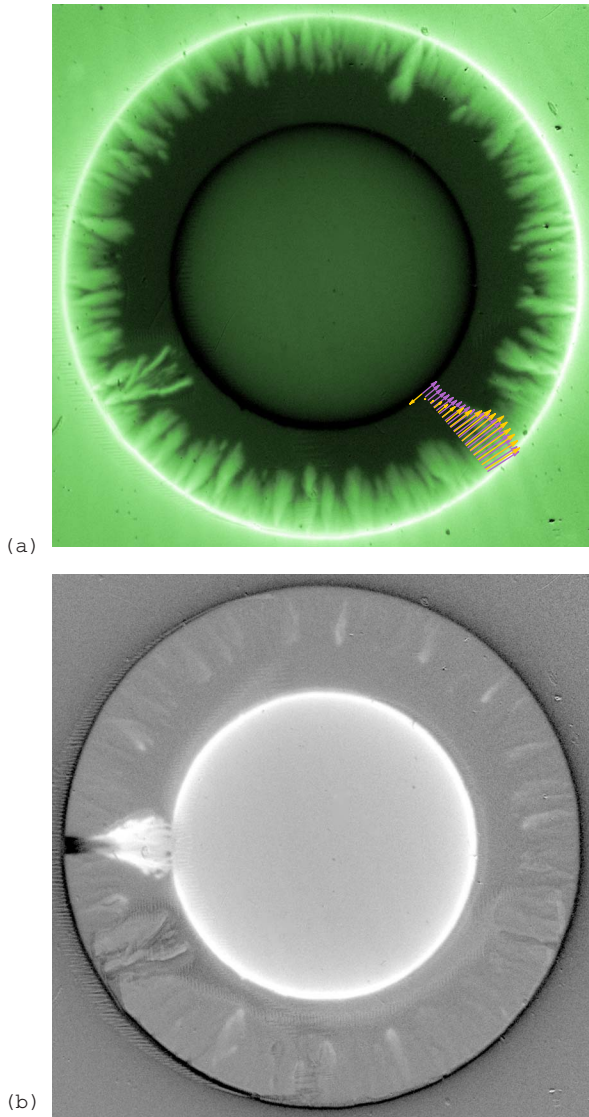


FIG. 1. (Color online) (a) A field map of the sample at $T = 6.2$ K and $B_a = 13$ mT. Bright pixels correspond to positive magnetic field, while dark pixels correspond to negative. Pixels in the Meissner region indicate the zero level. (b) The difference in field between the map shown here and the subsequent map in the sequence after a dendrite has perforated the ring and injected a large amount of flux into the central hole. Bright and dark pixels indicate flux has entered or left, respectively. Again the Meissner state indicate the zero level. While the most conspicuous feature is the large flux increase in the central hole, one can also observe a reduction in the field around the outer edge. In the superconducting material there is very little change in the field. The arrows superimposed on the field map show the current distributions before and after the perforation.

expected if Φ_{self} remained constant. This means there is some relaxation of the supercurrent in the ring as the applied field increases.

The central observation in this paper is seen in the curves obtained at temperatures below T_{th} . $\Phi_{r < r_p}$ is again zero up to a certain level, the perforation field, whereafter it increases in a steplike fashion, with sudden jumps followed by periods of

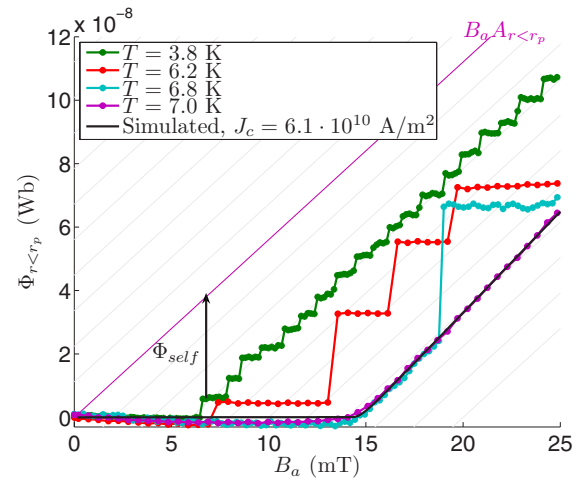


FIG. 2. (Color online) Measured flux within r_p as a function of applied field showing the crossover from complete screening to a linear increase following the applied field. The flux jumps are small and frequent at low temperature, becoming rarer and larger when the temperature approaches T_{th} . The oblique grid lines have slope $A_{r < r_p}$, with the line through the origin representing the contribution to $\Phi_{r < r_p}$ from the applied field. The contribution to the flux from the ring currents Φ_{self} is illustrated for one of the curves. The solid black line is the result of a simulation with a Kim model for the critical current (see Sec. V).

screening. At $T = 3.8$ K there are small and frequent jumps above the perforation field, which in this case is ≈ 6.5 mT. The average slope of the flux curve corresponds to the flux increase due to the applied field, but Φ_{self} is much smaller than for the usual critical state above T_{th} . This means that the avalanches reduce the average screening current flowing in the ring.

The curves at $T = 6.2$ and 6.8 K show similar behavior, but with larger and fewer jumps and a slightly larger perforation field. In the latter case the jump occurs well *after* the field of full penetration has been reached.

Clearly the flux jumps are accompanied by an abrupt reduction of the total ring current, with a recovery taking place during the screening phases. However, it is not only the total current which is affected, but also the current distribution. Using an efficient inversion scheme based on the Biot-Savart law which takes advantage of the fast Fourier transform,²² we obtain 2D current distributions from our measured magnetic field maps. Superimposed on the field map in Fig. 1(a) are two sets of arrows showing the direction and density of current just prior to and just after a perforation. In the former case the supercurrent is qualitatively what we expect in a critical state ring, with a saturated current in the flux penetrated part of the sample and a smaller screening current in the Meissner state region. The perforation profoundly changes this distribution. Near the outer edge there is a significant reduction in the current. Further from this edge, but within the flux penetrated region there is no discernible change in the current, while it is reduced throughout the Meissner region. However, the greatest change occurs close to the inner edge, where the current actually changes direction.

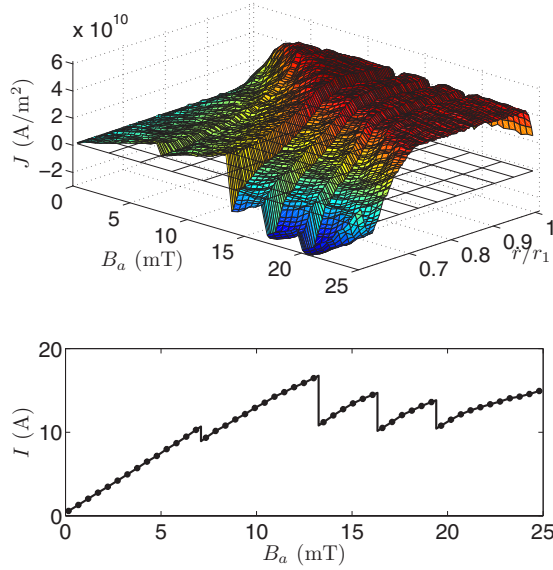


FIG. 3. (Color online) (top) The evolution of the current along the radial profile and for the same experiment shown in Fig. 1. (bottom) The total ring current obtained by integrating the current density across the ring width.

All these features are typical after perforation events. For the particular image sequence under discussion one can see the complete evolution of the current in Fig. 3. Each of the four perforations that occurred in the sequence are visible as distinct reductions in the current level, with most of the change occurring near the inner edge.

IV. PEAK TEMPERATURE AND DURATION OF THE PERFORATIONS

The experiments give accurate measurements of the state just before and just after perforations. Despite the fact that the dynamics is far too quick for our experimental setup, the fact that we *can* observe the change in $\Phi_{r < r_p}$ allows us to make some qualified inferences about the details of the process. The starting point is to split the process into two phases: (i) the nucleation and growth phase when the dendrite tip rapidly moves from the outer to the inner edge creating a heated channel and (ii) the flow phase when the resistive channel simultaneously impedes the supercurrents and injects flux into the central hole. We emphasize that during the first phase there should be little or no change in $\Phi_{r < r_p}$. Its duration is only determined by the dendrite tip velocity. Ultrafast MO measurements³⁷ has been used to measure the tip velocity of dendrites in MgB₂ yielding a value $v_{\text{tip}} = 10^5$ m/s. This tip velocity gives a crossing time $\delta t_1 = 10^{-8}$ s in our sample.

For a narrow ring or a uniform current distribution the evolution of the current during phase 2 can be expressed as a balance between the voltage drop RI across the heated channel and the induced emf voltage $L\dot{I}$ due to the change in the ring current:

$$L \frac{dI}{dt} + R(t)I = 0. \quad (3)$$

R is an Ohmic resistance which, depending on the stage of the process, results either from a normal state resistivity above the critical temperature T_c , or a flux flow resistivity originating from moving vortices. It is nonzero as long as the channel remains open. The inductance L is a property of the ring, and is only determined by the geometry. The Joule heating increases the temperature in the channel, a process which can be described by the heat equation

$$c \frac{dT}{dt} = \rho J^2 - \frac{h}{d}(T - T_0), \quad (4)$$

where we have ignored a term describing heat diffusion into the surrounding superconducting material. c is the heat capacity, h is the heat transfer coefficient to the substrate, and T_0 is the temperature of the substrate assumed to be equal to the cold finger temperature. The two equations are in fact coupled, since the current in the ρJ^2 term evolves according to Eq. (3). Moreover, the resistivity is strongly temperature dependent below T_c , and hence the evolution of the current is influenced by the channel temperature. Physically, one can think of the process in the following way: as phase 2 commences the ρJ^2 term dominates over the heat removal term leading to an increase in the temperature. But this has two consequences, both of which tend to oppose a further increase in temperature: first, the heat removal term becomes larger for higher temperature and secondly the current becomes smaller and hence the heat generation is reduced. At some point heat removal equalizes the heat generation and a maximum T is reached, after which the temperature decreases until the current density drops below J_c . At this point the resistivity vanishes, and the flux injection halts.

The fact that c , R , and h are all temperature dependent means an analytic solution is difficult to find. However, Eq. (4) can be used to estimate the maximum temperature during phase 2 directly by putting $dT/dt = 0$. Following Ref. 16 we write the heat transfer coefficient as $h(T) = h_0(T/T_c)^3$ and obtain the following equation for the maximum temperature T_{max} :

$$\frac{\rho J^2 d T_c^3}{h_0} = T_{\text{max}}^3 (T_{\text{max}} - T_0). \quad (5)$$

From Fig. 3 we find that at perforation the average current density over the whole ring is $J \approx 0.45 J_c = 2.7 \times 10^{10}$ A/m². The heat transfer coefficient was estimated in Ref. 16 to be $h_0 = 20$ kW/K m² on samples manufactured in the same way on the same sort of substrate as the current sample. If the temperature is moderately above T_c , the resistivity is independent of temperature in this material^{17,23,24} and can be taken as $\rho_n = 10^{-7}$ Ω m. Finally, with $T_c = 40$ K we obtain a peak temperature during the flux injection process of $T_{\text{max}} = 105$ K. We note that this solution is a unique solution of Eq. (5) for $T > T_0$ when realistic models of a temperature dependent flux flow resistivity is inserted in the left hand side.

We can now estimate the duration of phase 2 from Eq. (3). With the above temperature estimate in mind R is determined by the normal state resistivity $R = \rho_n w / A$. It follows that Eq. (3) describes a simple exponential decay of current $I(t)$

$=I_{\text{before}} \exp(-\rho_n w/AL)$ with I_{before} being the ring current just prior to the perforation. The area $A=45 \times 10^{-11} \text{ m}^2$ is the radial cross section of our sample, and w is the width of the resistive region (the dendrite core). For the jump in flux $\Delta\Phi_{\text{self}}=(I_{\text{after}}-I_{\text{before}})L$, we obtain the time scale for the flux flow phase as

$$\delta t_2 = \frac{LA}{w\rho} \ln\left(\frac{1}{1 - \Delta\Phi_{\text{self}}/\Phi_{\text{self}}}\right). \quad (6)$$

The plots in Fig. 2 can be used to estimate both the jump in Φ_{self} and the inductance L of the ring. In the critical state at $B_a=B_p$ the ring current density is J_c everywhere, so the total current is $J_c A$. Since the flux due to the applied field is exactly cancelled by the supercurrents, we have $\Phi_{\text{self}}=B_p A_{r<r_p}$, and we find the inductance $L=B_p A_{r<r_p}/J_c A=4 \text{ nH}$. From the first jumps we estimate $\Delta\Phi_{\text{self}}/\Phi_{\text{self}}=0.2$. Notice that we now are concerned with the self-flux of the ring and consequently the contribution from the applied field must be subtracted in the curves in Fig. 2. The width w of the resistive region can be estimated from the core width of the dendrites. Barkov *et al.*²⁵ found that typically $w=10^{-5} \text{ m}$. With the normal state resistivity used in the temperature estimate we obtain $\delta t_2 \approx 4 \times 10^{-7} \text{ s}$. We stress that this estimate represents a lower bound on the true timescale. This is because the temperature is below T_c during part of the process, with a flux flow resistivity ρ_f which may be orders of magnitude smaller than the ρ_n we used to estimate the duration. However, most of the current change should occur when the resistivity is highest, i.e., $\rho=\rho_n$, and our δt_2 based on a constant resistivity is expected to be accurate.

In ignoring the term in Eq. (4) which describes heat diffusion into the surrounding superconducting material, we neglect a possible source of heat loss which would lead to a lower maximum temperature. With such a term, Eqs. (3) and (4) can be solved numerically to yield the complete temperature evolution as well as the width of the resistive region with only a single input from our experiments, namely, the change in flux $\Phi_{r<r_p}$. However, the calculation requires temperature dependent model parameters and detailed initial conditions for phase 2, which are known only approximately. We therefore believe our approximate solution is as reliable as such a full scale model would be.

V. CURRENT PROFILES DUE TO PERFORATIONS

In the discussion up to this point we have disregarded the non-uniform change in the current distribution which was pointed out in Sec. III. In this section we calculate the current distribution resulting from a perforation within the resistive channel model, and find that key features of the observations can be reproduced. The calculation scheme consists in computing the critical state of the ring up to some pre-defined applied field where a counter current is injected, reducing the total current and changing the current distribution. The trick is similar to the one used in recent work on flux focusing in superconducting quantum interference devices with a narrow slit.^{26,27} It is motivated by the desire to retain the tractable cylindrical symmetry: the counter current pro-

vides a simple way to model the effect of the resistive slit without sacrificing the symmetry, and without considering the dynamical details of the process.

The counter current distribution should leave the field inside the superconducting material unchanged in line with the observation from Fig. 1(b), a constraint which is fulfilled by a transport Meissner current for a ring. Of course, it is difficult in practice to impose a pure transport current on a ring: therefore this problem has received no attention in the literature so far, in contrast to the analogous problem of a flat strip with a transport current.²⁸⁻³⁰

The calculations of the field and current distributions are inspired by the works of Brandt,³¹⁻³⁴ which details an efficient numerical method to model the electrodynamics in flat superconductors. The starting point is Maxwells equations, written as $\nabla^2 \mathbf{A} = \mu_0 \mathbf{J}$, and a suitable material law describing the superconducting material $E=E_c(J/J_c)^n$; E is the electric field, J is the current, J_c is the critical current of the superconductor, E_c is a critical electric field, and n is the creep exponent. While this E - J law describes flux creep, it is conveniently used in numerical calculations to describe the critical state if the exponent n is high enough. These two equations lead to an equation of motion for the current (see Refs. 32 and 33 for details) which can be written in cylindrical coordinates as

$$j(r) = \frac{1}{\mu_0} \int_{r_0}^{r_1} Q^{-1}(r, r') \left(J(r')^n \frac{E_c}{J_c d} - \frac{r}{2} \dot{B}_a \right) dr'. \quad (7)$$

B_a is the applied field. The integral kernel $Q(r, r')$ is given by

$$Q(r, r') = \frac{1}{2\pi} \int_0^\pi \frac{r' \cos \phi}{\sqrt{r^2 + r'^2 + 2rr' \cos \phi}} d\phi \quad (8)$$

and relates the magnetic vector potential $A(r)$ everywhere to the current $J(r')$ in the ring via

$$A = \mu_0 \int_{r_0}^{r_1} Q(r, r') J(r') dr'. \quad (9)$$

We integrate Eq. (7) numerically in a straightforward manner. The kernel is found by computing Eq. (8) at discrete points using a nonequidistant grid with high grid density near the sample edges.³³ The ensuing matrix is then inverted to obtain $Q^{-1}(r, r')$ required in Eq. (7). A technical challenge with this formulation is that $Q(r, r')$ diverges for $r=r'$, but this can be handled by carefully selecting finite diagonal elements (see the Appendix for more details).

The magnetic field distribution is calculated from $J(r)$ by first computing the vector potential from Eq. (9), and inserting this into $B(r)=\partial A(r)/\partial r + A(r)/r + B_a$. The computed flux $\Phi_{r<r_p} = \int_S B dS = 2\pi \int_0^r B(r') r' dr'$ is shown in Fig. 2, and agrees well with the experimental curves. To achieve this close matching it is necessary to include a field dependent critical current in the simulations. We used a Kim model $J_c = J_{c0}/(1 + |B|/B_K)$, with $B_K=80 \text{ mT}$. This value is only a little higher than expected based on previously reported²⁴ magnetization data on the same sort of samples.

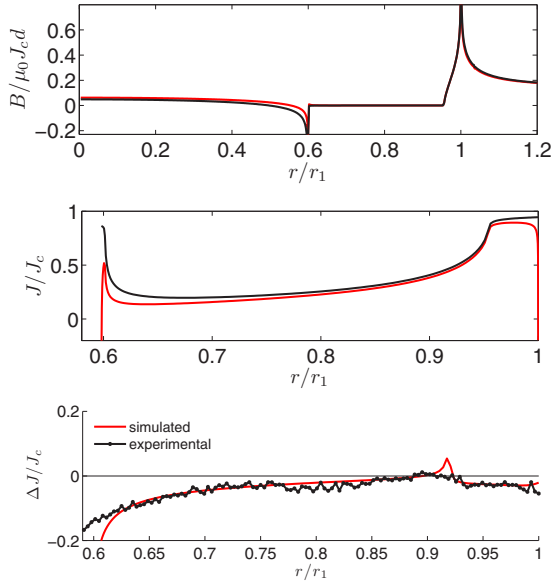


FIG. 4. (Color online) Field (top) and current (middle) profiles just prior to and just after a simulated perforation. The perforation field was $0.19 \mu_0 J_c d$, the creep exponent $n=30$, the blocking parameter $\alpha=0.13$, and a field independent J_c was used. (Bottom) The change in current due to a perforation. The solid gray (red online) line is results from a simulation, and the black line is experimental points. The plot shows that the simulations reproduce the change well. In particular, the change in current grows as one gets closer to the inner edge.

In order to complete the perforation model we also need the distribution of a Meissner transport current in this cylindrical symmetry. This may be found by inverting Eq. (9) to find the current $J(r)$ from a magnetic potential $A(r)$. With $A(r)=K/r$ the magnetic field inside the superconducting material is zero, so the desired current distribution can be expressed as

$$J_{\text{tr}}(r) = \frac{K}{\mu_0} \int_{r_0}^{r_1} \frac{Q^{-1}(r, r')}{r'} dr'. \quad (10)$$

It is convenient to choose the constant K such that the total transport current equals the total shielding current at perforation, i.e., that $\int J_{\text{tr}}(r) dr = \int J_{\text{before}}(r) dr$. The net current just after a perforation can then be written

$$J_{\text{after}}(r) = J_{\text{before}}(r) - \alpha J_{\text{tr}}(r). \quad (11)$$

The parameter $\alpha \in [0, 1]$ determines the reduction of the total ring current as a result of a perforation. This α is analogous to the relative change in flux $\alpha' = \Delta\Phi_{\text{self}} / \Phi_{r < r_p}$ in the simplified model described in Sec. IV. We artificially inject this current at a predetermined applied field, and subsequently let the simulation proceed normally, i.e., according to Eq. (7) again. Figure 4 shows field and current profiles just before and shortly after a perforation. We observe that most of the current change occurs near the inner edge. In the Meissner region there is some noticeable reduction in the current closer to the inner flux front, but towards the outer flux front there is hardly any change at all. Near the outer

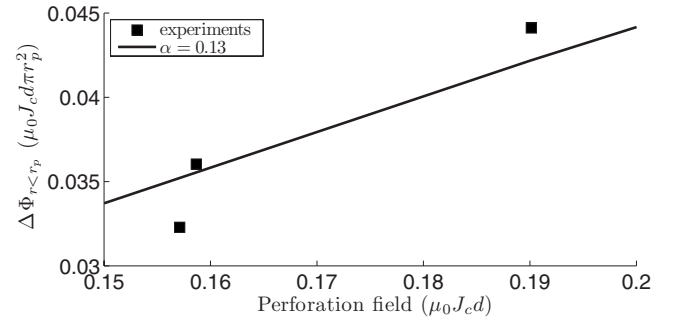


FIG. 5. Flux jump size versus perforation field from simulations and experiments. The filled squares show experimental first jumps, and the solid line shows results from simulations with $\alpha=0.13$. The simulations reproduce the experimental fact that the current is reduced by a smaller amount than $\Phi_{r < r_p}$

edge, though, the current has decreased considerably. These features are summarized in the bottom plot of Fig. 4, which also shows that the simulations reproduce the key features of the experimentally observed changes.

In Fig. 5 we show computed values of flux jump sizes versus the perforation field for different values of the blocking parameter α . Also included in the plot is the first jump in some experiments. The plot shows that the total ring current is reduced by approximately 13% by perforations. This is considerably smaller than the reduction we would infer from the plots of $\Phi_{r < r_p}$ in Fig. 2 using $\Phi = LI$, where the relative change in the flux is ≈ 0.2 for the first jumps. This is of course due to the fact that most of the current change occurs near the inner edge where the effect on the flux in the central hole is greatest. The value $\alpha=0.13$ is also more in line with the plot of total current in Fig. 3, which shows a relative change in current of ≈ 0.16 for the first jump.

VI. CONCLUSION

We have proposed a method to estimate the temperature rise during dendritic avalanches in superconducting thin films. This is accomplished using MO imaging to measure the flux change in the central hole of a superconducting MgB₂ ring caused by avalanches stretching from the outer to the inner edges of the ring. Our model assumes that the dendrite tip creates a short-lived, resistive heated channel as it crosses the ring, injecting flux into the central hole. From this model we are able to estimate the peak temperature during flux injection to be $T_{\text{max}} = 2.5T_c = 105$ K, the duration of process to be $\delta t = 4 \times 10^{-7}$ s, and calculate the current profiles before and after injection events.

ACKNOWLEDGMENTS

We thank Paul Leiderer for doing ultrafast MO imaging on MgB₂ samples following our request. Å.A.F.O., D.S., and T.H.J. gratefully acknowledge the financial support from FUNMAT@UiO and the Research Council of Norway.

APPENDIX: STABILITY OF THE NUMERICAL CALCULATIONS

The stability of the numerical calculations described in Sec. V hinges on a careful selection of finite replacement elements for the diverging diagonal terms in the kernel, Eq. (8). The problem has been dealt with in various ways previously.^{31,34–36} One way to obtain diagonal elements that work is the following: With an appropriate grid r_i and corresponding weights w_i one can integrate Q numerically over the ring width:

$$\int_{r_0}^{r_1} Q(r, r') dr' \approx \sum_i Q_{ij} w_i. \quad (\text{A1})$$

The right hand side can be split into diagonal and off-diagonal terms, and the equation can be rewritten as

$$Q_{ii} w_i = \int_{r_0}^{r_1} Q(r, r') dr' - \sum_{i \neq j} Q_{ij} w_i. \quad (\text{A2})$$

The integral of $Q(r, r')$ over r' can be carried out by changing the order of integration of ϕ and r' . The r' integration can be done analytically; the result is a smooth integrand for the ϕ integration except for a singularity at $\phi = \pi$, but the integral is well defined over the entire interval $\phi \in [0, \pi]$. Equation (8) can be used to compute the off-diagonal elements on the right hand side, and the resulting

set of diagonal elements give stable and accurate computations.

An additional numerical challenge comes from the fact that J_{tr} obtained from Eq. (10) diverges at the edges. One way to cope with this for a regular Bean model (no field dependent J_c) is to modify the E - J law so that for current above $|J_c|$ there is an Ohmic resistivity ρ_f in mathematical form that

$$E = \begin{cases} \rho_f J & \text{if } J > J_c, \\ E_c \left| \frac{J}{J_c} \right|^n \text{sgn}(J) & \text{if } J \leq J_c. \end{cases} \quad (\text{A3})$$

With this small modification the supercritical currents quickly relax in the simulations.

The resistivity does not necessarily have a physical meaning in this context since its main purpose is to stabilize the simulation when the current reaches extremely large values. Still, such an Ohmic resistivity is realistic in superconductors for currents larger than the critical current, and the use of the modified E - J law is reasonable also from a physical point of view. We use a $\rho_f/\mu_0 = 0.001 \text{ s}^{-1}$. The value will in reality depend on magnetic field since it captures the motion of vortices—the more vortices moving will generate a larger electric field acting against the current. However, for the computations the exact value is not crucial provided it is small.

*a.a.f.olsen@fys.uio.no

†t.h.johansen@fys.uio.no

- ¹P. Leiderer, J. Boneberg, P. Brüll, V. Bujok, and S. Herminghaus, Phys. Rev. Lett. **71**, 2646 (1993).
- ²V. Bujok, P. Brüll, J. Boneberg, S. Herminghaus, and P. Leiderer, Appl. Phys. Lett. **63**, 412 (1993).
- ³C. A. Durán, P. L. Gammel, R. E. Miller, and D. J. Bishop, Phys. Rev. B **52**, 75 (1995).
- ⁴I. A. Rudnev, S. V. Antonenko, D. V. Shantsev, T. H. Johansen, and A. E. Primenko, Cryogenics **43**, 663 (2003).
- ⁵M. S. Welling, R. J. Westerwaal, W. Lohstroh, and R. J. Wijngaarden, Physica C **411**, 11 (2004).
- ⁶S. C. Wimbush, B. Holzapfel, and C. Jooss, J. Appl. Phys. **96**, 3589 (2004).
- ⁷I. A. Rudnev, D. V. Shantsev, T. H. Johansen, and A. E. Primenko, Appl. Phys. Lett. **87**, 042502 (2005).
- ⁸M. Menghini, R. J. Wijngaarden, A. V. Silhanek, S. Raedts, and V. V. Moshchalkov, Phys. Rev. B **71**, 104506 (2005).
- ⁹T. H. Johansen, M. Baziljevich, D. V. Shantsev, P. E. Goa, Y. M. Galperin, W. N. Kang, H. J. Kim, E. M. Choi, M.-S. Kim, and S. I. Lee, Semicond. Sci. Technol. **14**, 726 (2001).
- ¹⁰Z. W. Zhao, S. L. Li, Y. M. Ni, H. P. Yang, Z. Y. Liu, H. H. Wen, W. N. Kang, H. J. Kim, E. M. Choi, and S. I. Lee, Phys. Rev. B **65**, 064512 (2002).
- ¹¹P. S. Swartz and C. P. Bean, J. Appl. Phys. **39**, 4991 (1968).
- ¹²R. G. Mints and A. L. Rakhmanov, Rev. Mod. Phys. **53**, 551 (1981).
- ¹³R. G. Mints and E. H. Brandt, Phys. Rev. B **54**, 12421 (1996).

- ¹⁴I. S. Aranson, A. Gurevich, M. S. Welling, R. J. Wijngaarden, V. K. Vlasko-Vlasov, V. M. Vinokur, and U. Welp, Phys. Rev. Lett. **94**, 037002 (2005).
- ¹⁵D. V. Denisov, A. L. Rakhmanov, D. V. Shantsev, Y. M. Galperin, and T. H. Johansen, Phys. Rev. B **73**, 014512 (2006).
- ¹⁶D. V. Denisov, D. V. Shantsev, Y. M. Galperin, E.-M. Choi, H.-S. Lee, S.-I. Lee, A. V. Bobyl, P. E. Goa, A. A. F. Olsen, and T. H. Johansen, Phys. Rev. Lett. **97**, 077002 (2006).
- ¹⁷W. N. Kang, H.-J. Kim, E.-M. Choi, C. U. Jung, and S.-I. Lee, Science **292**, 1521 (2001).
- ¹⁸E. M. Choi, H. S. Lee, H. J. Kim, B. Kang, S. I. Lee, A. A. F. Olsen, D. V. Shantsev, and T. H. Johansen, Appl. Phys. Lett. **87**, 152501 (2005).
- ¹⁹M. Baziljevich, A. V. Bobyl, D. V. Shantsev, E. Altshuler, T. H. Johansen, and S. I. Lee, Physica C **369**, 93 (2002).
- ²⁰C. Jooss, J. Albrecht, H. Kuhn, H. Kronmüller, and S. Leonhardt, Rep. Prog. Phys. **65**, 651 (2002).
- ²¹Åge Andreas Falnes Olsen, T. H. Johansen, D. Shantsev, E.-M. Choi, H.-S. Lee, H. J. Kim, and S.-I. Lee, Phys. Rev. B **74**, 064506 (2006).
- ²²B. J. Roth, N. G. Sepulveda, and J. John P. Wikswo, J. Appl. Phys. **65**, 361 (1989).
- ²³C. B. Eom *et al.*, Nature (London) **411**, 558 (2001).
- ²⁴H.-J. Kim, W. N. Kang, E.-M. Choi, M.-S. Kim, K. H. P. Kim, and S.-I. Lee, Phys. Rev. Lett. **87**, 087002 (2001).
- ²⁵F. L. Barkov, D. V. Shantsev, T. H. Johansen, P. E. Goa, W. N. Kang, H. J. Kim, E. M. Choi, and S. I. Lee, Phys. Rev. B **67**, 064513 (2003).

- ²⁶A. A. Babaei Brojeny and J. R. Clem, Phys. Rev. B **68**, 174514 (2003).
- ²⁷E. H. Brandt, Phys. Rev. B **72**, 024529 (2005).
- ²⁸W. T. Norris, J. Phys. D **3**, 489 (1970).
- ²⁹E. Zeldov, J. R. Clem, M. McElfresh, and M. Darwin, Phys. Rev. B **49**, 9802 (1994).
- ³⁰E. H. Brandt and M. Indenbom, Phys. Rev. B **48**, 12893 (1993).
- ³¹E. H. Brandt, Phys. Rev. B **50**, 4034 (1994).
- ³²E. H. Brandt, Phys. Rev. B **54**, 4246 (1996).
- ³³E. H. Brandt, Phys. Rev. B **55**, 14513 (1997).
- ³⁴E. H. Brandt, Phys. Rev. B **58**, 6506 (1998).
- ³⁵E. H. Brandt and J. R. Clem, Phys. Rev. B **69**, 184509 (2004).
- ³⁶J. Gilchrist and E. H. Brandt, Phys. Rev. B **54**, 3530 (1996).
- ³⁷P. Leiderer (private communication).